



### **Science Arts & Métiers (SAM)**

is an open access repository that collects the work of Arts et Métiers Institute of Technology researchers and makes it freely available over the web where possible.

This is an author-deposited version published in: <https://sam.ensam.eu>  
Handle ID: <http://hdl.handle.net/10985/18362>

#### **To cite this version :**


Alexandre MESSAGER, Arnaud JUNET, Thierry PALIN-LUC, Jean-Yves BUFFIERE, Mohamed EL MAY, Yves GAILLARD, Andrew KING, Anne BONNIN, Yves NADOT, Nicolas RANC, Nicolas SAINTIER - In situ synchrotron ultrasonic fatigue testing device for 3D characterisation of internal crack initiation and growth - Fatigue and Fracture of Engineering Materials and Structures - Vol. 43, n°3, p.558-567 - 2020

Any correspondence concerning this service should be sent to the repository

Administrator : [scienceouverte@ensam.eu](mailto:scienceouverte@ensam.eu)



# In situ synchrotron ultrasonic fatigue testing device for 3D characterisation of internal crack initiation and growth

Alexandre Messenger<sup>1</sup> | Arnaud Junet<sup>2</sup> | Thierry Palin-Luc  | Jean-Yves Buffiere<sup>2</sup> |  
Nicolas Saintier<sup>1</sup> | Nicolas Ranc<sup>3</sup> | Mohamed El May<sup>1</sup> | Yves Gaillard<sup>4</sup> |  
Andrew King<sup>5</sup> | Anne Bonnin<sup>6</sup> | Yves Nadot<sup>7</sup>

<sup>1</sup> Arts et Métiers ParisTech, I2M Bordeaux, CNRS, Université de Bordeaux, Esplanade des Arts et Métiers, Talence, France

<sup>2</sup> INSA-Lyon, MATEIS, CNRS, Villeurbanne, France

<sup>3</sup> Arts et Métiers ParisTech, PIMM, CNRS, Paris, France

<sup>4</sup> Centre Technique des Industries de la Fonderie (CTIF), Sèvres Cedex, France

<sup>5</sup> Synchrotron SOLEIL, L'Orme des Merisiers Saint-Aubin, Gif-sur-Yvette, France

<sup>6</sup> Swiss Light Source, Paul Scherrer Institut, Villigen, Switzerland

<sup>7</sup> Institut PPRIME ISAE-ENSMA, CNRS, Université de Poitiers, Futuroscope Chasseneuil Cedex, France

## Correspondence

Thierry Palin-Luc, Arts et Métiers ParisTech, I2M Bordeaux, CNRS, Université de Bordeaux, Esplanade des Arts et Métiers, 33405 Talence, France.  
Email: thierry.palin-luc@ensam.eu

## Funding information

Agence Nationale de la Recherche, Grant/Award Number: ANR-16-CE08-0039-03

## Abstract

This work presents a new ultrasonic fatigue testing device for studying the initiation and propagation mechanisms of internal microstructurally short fatigue cracks using in situ synchrotron tomography. Its principle is described as well as the method used for automatically detecting crack initiation and its subsequent growth. To promote internal crack initiation, specimens containing internal casting defects were tested between the high cycle and very high cycle fatigue regimes ( $10^7$ - $10^9$  cycles). Preliminary results show the ability of this new device to initiate an internal microstructurally short crack in a reasonable testing time and monitor its growth.

## KEYWORDS

aluminum alloy, internal short crack growth, fatigue test, synchrotron radiation, X-ray tomography

## 1 | INTRODUCTION

Casting is a widely used industrial process allowing to produce geometrically complex components with relatively low production costs. However, this manufacturing process produces casting defects (such as pores, oxides, or

shrinkages) inducing local stress concentrations and consequently a lower fatigue resistance compared with wrought alloys. Several authors have highlighted the fatigue strength reduction because of the presence of defects<sup>1-5</sup>. Numerous studies have used X-ray microtomography for studying crack propagation mecha-

**Nomenclature:** A, area of the defect projected on the plane perpendicular to the loading axis; HCF, high cycle fatigue; LCF, low cycle fatigue; N, number of cycles;  $N_i$ , number of cycles in the  $i$ th loading sequence;  $N_{Tot}$ , total number of cycles;  $U_1$ , amplitude of the fundamental frequency of the displacement of the specimen extremity;  $U_2$ , amplitude of second harmonic of the displacement of the specimen extremity; VHCF, very high cycle fatigue;  $\beta$ , non-linearity damage parameter;  $\Delta T$ , temperature variation

nisms<sup>6,7</sup> or damage development<sup>8</sup>. But only very few works either in low cycle fatigue (LCF)<sup>9,10</sup> or high cycle fatigue (HCF)<sup>11,12</sup> have been published on internal crack initiation and propagation monitoring with a nondestructive technique.

These studies show that (i) both internal and external cracks can initiate in the same specimen and (ii) surface crack growth rates are higher than internal ones. Surface cracks prevail over internal ones in LCF and HCF regimes, that is the main reason why only restricted observations of internal crack propagation<sup>9,11,12</sup> have been done so far but this is different in very high cycle fatigue (VHCF) regime where internal cracks dominate. Furthermore, there are only very limited experimental data of internal crack growth rate available at the moment.<sup>9,11,12</sup> Several authors<sup>13-15</sup> have already underlined that internal failure can be promoted by low stress loadings leading to a very large number of cycles to failure. Such tests, in the VHCF regime, can be performed in a realistic testing time using ultrasonic testing machine.

These machines are based on the vibration, at approximately 20 kHz, of their components which are excited by a piezoelectric converter.<sup>16</sup> Even if all physical reasons are not well-known, most researchers agree that internal crack initiation is due to the very high number of fatigue cycles applied at a very low stress level.<sup>17,18</sup> As a matter of fact, internal crack initiation in the VHCF regime has been observed at lower loading frequencies (10-100 Hz).<sup>19,20</sup> Several authors have shown that acoustic measurements allow to monitor damage accumulation in fatigue specimens<sup>21-23</sup>. During ultrasonic fatigue tests, the piezoelectric converter produces the ultrasonic stationary wave, which generates the cyclic loading<sup>19</sup>. Dislocations and cracks interfere with this ultrasonic wave, thus, generating higher harmonics than the fundamental one.<sup>24</sup> This distortion of the ultrasonic signal can be measured through modal analysis.<sup>25</sup> Such in situ monitoring techniques have been used, for example, on aluminum alloy,<sup>26</sup> Ti6Al4V, and 2000 series Al specimens<sup>27</sup> to detect crack initiation. Moreover, infrared thermal analysis has also been used to characterize fatigue crack initiation in cast aluminum alloys and steels.<sup>28,29</sup> Nevertheless, all those studies used a postmortem analysis with no direct evidence of internal crack initiation.

The purpose of this work is to study in-situ the 3D initiation and propagation of internal microstructurally short fatigue cracks (named short crack in the following) using synchrotron X-ray phase contrast tomography, modal analysis and infrared thermal analysis. For promoting internal fatigue crack initiation, the fatigue tests were conducted between the HCF and VHCF regimes at 20 kHz on specimens with internal artificial defects. An

automatic crack initiation detection system based on real time FFT processing has been developed for stopping the cyclic loading in the early stage of internal short fatigue crack initiation and subsequently allows 3D imaging.

## 2 | EXPERIMENTAL TESTING DEVICE

### 2.1 | Principle

An ultrasonic fatigue testing machine was developed in order to perform in situ synchrotron fatigue tests (see Figure 1). The ultrasonic part of the machine is a “classical” setup<sup>19</sup> composed of a piezoelectric converter powered by an ultrasonic generator and cooled by compressed air (in grey on Figure 1). A horn is used to mechanically amplify the ultrasonic signal generated by the piezoelectric converter. This machine is connected to a mechanical system in order to apply a quasi-static load to hold the crack open during imaging (in yellow on Figure 1). The horn vibration node is set on top of the static loading system, which is composed of a worm wheel driven by a stepper motor able to produce 1 kN load with  $\pm 1$  N accuracy. The loading system is displacement controlled; the force imposed to the specimen is monitored by a load sensor. In the experiments reported in this paper, the static load used to open the internal cracks during imaging was 80% of the maximum stress applied under cyclic loading at 20 kHz. The specimen stays at the same place for imaging under static load and cycling: a crucial issue for analyzing the series of 3D images which do not need to be realigned.

This testing machine was used in continuous mode, ie, without pulse-pause, for carrying out the experiments presented in this paper. However, the software is able to operate in pulse-pause mode to avoid a possible self-heating of the specimen as observed for instance for some steels.<sup>30</sup> The specimen can also be cooled by using an air gun with dry compressed air. Cooling was not needed in this work.

The specimen geometry is designed to vibrate in a tension compression mode at  $20 \pm 0.5$  kHz and its extremities adapted to the static loading system (Figure 2).

### 2.2 | Instrumentation of the testing device

A Polymethylmethacrylate (PMMA) tube makes a full 360° tomographic scan possible without missing views. An aperture in the upper part of the tube supporting the horn allows the observation of the mat black painted specimen with an infrared camera (FLIR SC4000). Likewise, an aperture in the lower part of the loading system

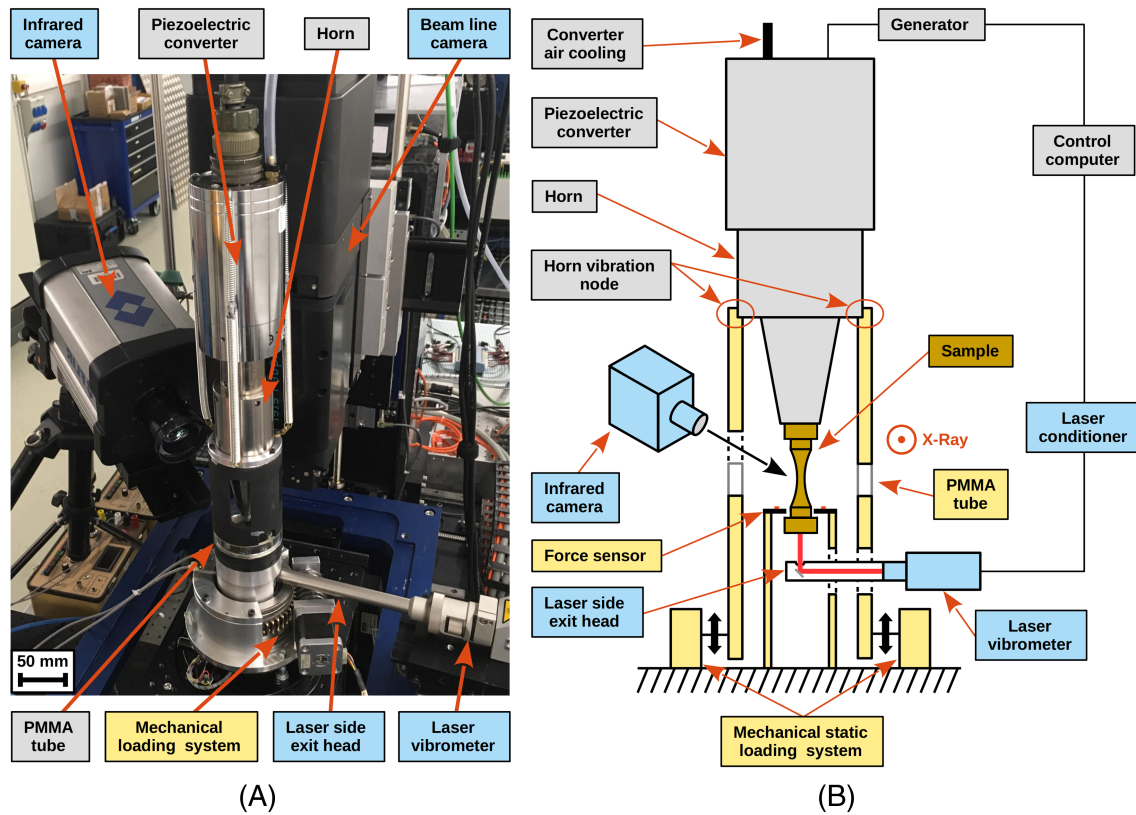


**FIGURE 1** (A) Picture of the in situ synchrotron experimental setup as installed at the TOMCAT beamline at Swiss light source (SLS), (B) scheme of this setup with the in situ ultrasonic fatigue machine (in grey), static loading system (in yellow) and its instrumentation (in blue). The mass of the machine installed on the synchrotron rotation stage is approximately 6 kg [Colour figure can be viewed at [wileyonlinelibrary.com](http://wileyonlinelibrary.com)]

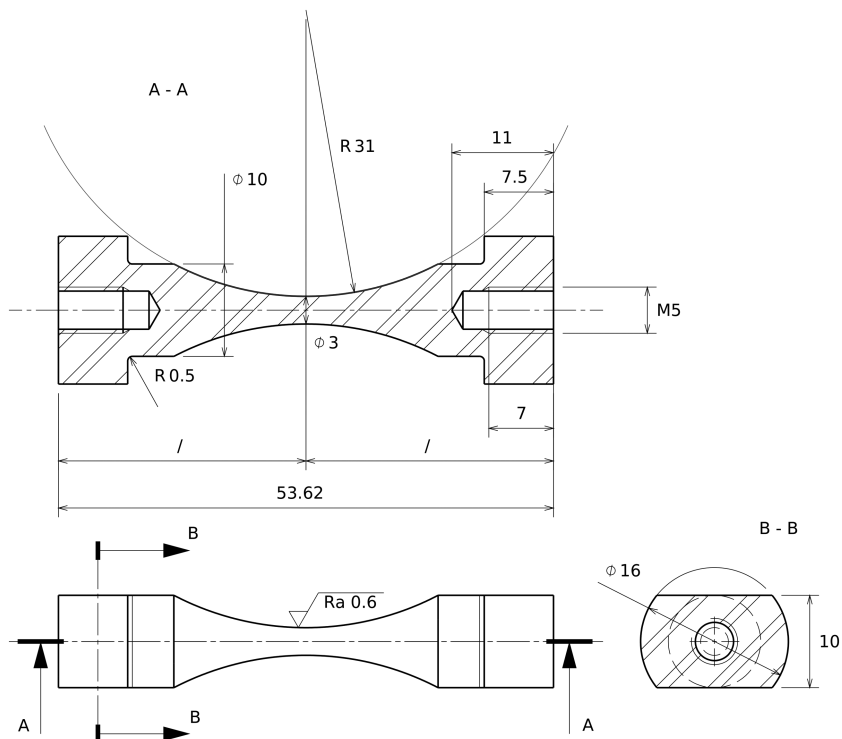


**FIGURE 2** Specimen geometry (dimensions in mm)

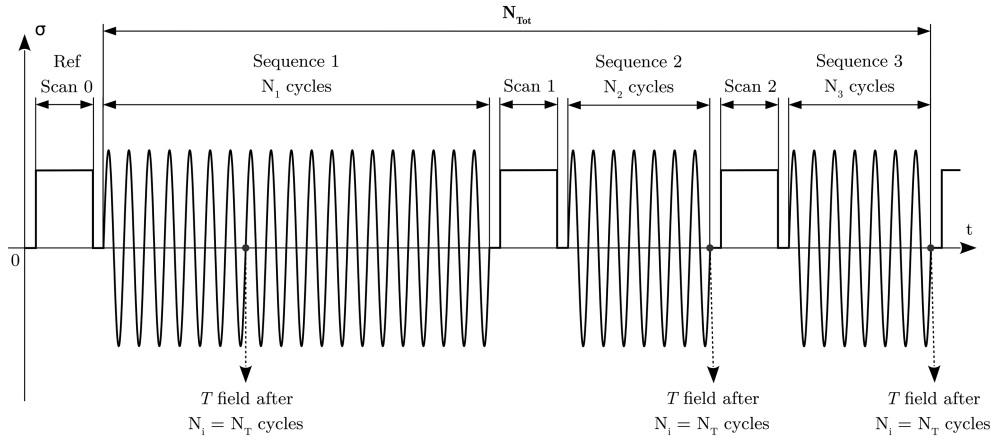


**FIGURE 3** Schematic illustration of the testing procedure

allows measurement of the velocity of the free standing extremity of the specimen with a laser vibrometer. The velocity signal given by this vibrometer is treated by a real-time FFT routine implemented in a Polytec data acquisition system. The laser conditioner is directly linked to the ultrasonic testing machine controller allowing to automatically interrupt the fatigue test when the amplitude of the second harmonic, at approximately 40 kHz, exceeds a predefined adjustable value.

## 2.3 | Testing procedure

The crack initiation detection and propagation monitoring procedure is as follows. First, a reference tomographic scan is recorded. An ultrasonic fatigue test is conducted under fully reversed loading until the real-time FFT system detects crack initiation and automatically interrupts the fatigue test. During this stage (and all the other ones as explained later), an infrared camera monitors the temperature field in the specimen central part. When the fatigue test is interrupted, a tomographic scan of the specimen under static load is carried out to confirm the presence of a crack. If no crack is visible in the reconstructed volume (test stop due to noisy signal was rare but possible\*), cycling is resumed until the system detecting crack initiation is triggered again and so on until a crack is visible in the reconstructed volume.

Then a crack propagation stage starts under the same loading conditions for a given number of cycles. During every propagation sequence, the temperature in the

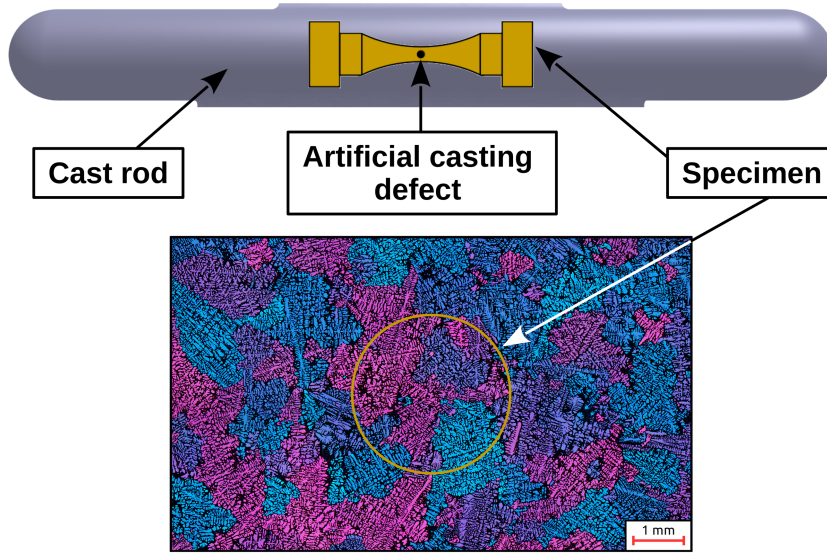
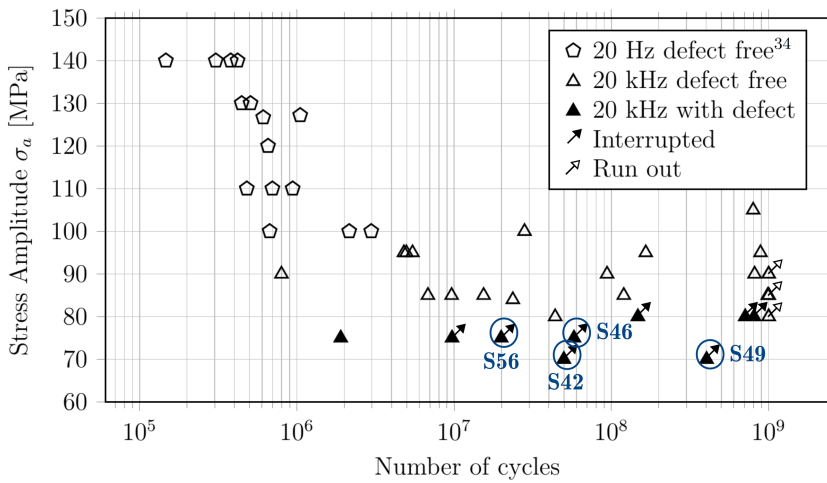
central part of the specimen is monitored by the infrared camera and the real time FFT analysis is also carried out. The aim of the temperature measurements is to record the temperature increase due to both mesoscopic plasticity and cyclic plasticity when a crack initiates and propagates as reported for instance by Krewerth et al<sup>28</sup> and Wagner et al.<sup>29</sup> At the end of each propagation sequence, a tomographic scan of the specimen gauge volume is performed to observe the crack propagation increment. This sequence is repeated several times (Figure 3). The number of cycles of the propagation sequences can be adapted depending on the crack progression. Because of the high loading frequency, most of the test duration corresponds to the tomography scan (between 5 and 10 min depending on the beam line) and preliminary data treatment (the cyclic loading only needs 5 s at 20 kHz for  $10^5$  cycles against approximately 1 h 23 min at 20 Hz, whereas reconstruction of a full volume takes around 20 min). The infrared camera has an acquisition frequency of 30 Hz with a 20-mK NETD (noise equivalent temperature difference) at 20°C and an exposure time of 450  $\mu$ s.

Two synchrotron X-ray tomography setups have been used: one at Tomcat beamline (SLS) and one at PSICHE beamline (SOLEIL); a detailed description of the two setups can be found in the papers by King et al<sup>31</sup> and Lovric et al.<sup>32</sup> The tomographic scans were recorded with a specimen to detect the distance of the order of 15 cm. With this relatively large distance, imposed by the machine, on both beamlines, a significant amount of phase contrast is obtained on the projections thanks to the large spatial coherence of the beam. This allows to image the eutectic silicon particles in the Al matrix and, more importantly, increases crack detection. On Tomcat beamline, the voxel size used (1.6  $\mu$ m) allows to image the whole section of the sample at the defect vicinity and radiographs are recorded during a 180° rotation. At PSICHE, one 360 degree rotation with the rotation axis off center is used (half acquisition configuration). A

\*The real-time FFT analysis of the velocity signal is not used as a monitoring technique itself but as a detecting technique only. The nonpositive detection is because of the very high sensitivity of the laser velocimeter. For instance, a small parasitic vibration or shock on the laboratory ground is enough for a nonpositive stop. Although the sample environment in the experimental hutch is very stable, from the experience of the authors, such variations are almost unavoidable!

**TABLE 1** Imaging conditions used at TOMCAT and PSICHE beamlines (FOV = field of view in pixels × pixels)

Beamline	Beam Configuration	Energy	Number of Views	Exposure Time	FOV	Voxel Detector Size
TOMCAT	Multilayer	30 keV	2501	70 ms	2560 × 2160	1.6 μm
PSICHE	Filtered white beam	29 keV	3900	20 ms	2750 × 2048	1.3 μm

**FIGURE 4** (Top) Schematic drawing of the specimen location in the cast rod with the artificial defect, (bottom) picture of the microstructure with an optical microscope after electropolishing and chemical etching with the Barker's reagent [Colour figure can be viewed at wileyonlinelibrary.com]**FIGURE 5** Experimental data in a SN diagram for the cast AlSi7Mg0.6 alloy under tension ( $R = -1$ ) on defect-free specimen at 20 Hz 2014 at 20 kHz (this study) on defect free specimen and specimen with artificial internal defect [Colour figure can be viewed at wileyonlinelibrary.com]

multilayer at Tomcat and a filtered white beam at PSICHE provide enough flux to reduce efficiently the exposure time (70 and 20 ms, respectively) and obtain scanning times of the order of 5 minutes. A classical filtered back projection reconstruction algorithms was used to obtain the 3D images because it gives better results than the Paganin approach for reconstructing the phase with a single distance. The detailed imaging conditions used on each beamline are summarized in Table 1

The amplitude of the second harmonic,  $U_2$ , of the displacement<sup>†</sup> at the free specimen end is checked in real

<sup>†</sup>Obtained by integrating the velocity signal measured by the laser vibrometer.

time for detecting crack initiation but also recorded together with the amplitude of the fundamental,  $U_1$ , to compute a non-linear parameter,  $\beta$ , representative of the damage accumulation in the specimen under cyclic loading as proposed by Kumar et al<sup>26</sup>:

$$\beta = 20 \log_{10} \left( \frac{U_2}{U_1} \right) - 20 \log_{10} \left( \frac{U_2}{U_1} \right)_0 \quad (1)$$

The value of this parameter is normalized by its value at the beginning of the fatigue tests when the specimen is undamaged (0 subscript in Equation 1). After the test, crack propagation can be eventually analyzed using X-

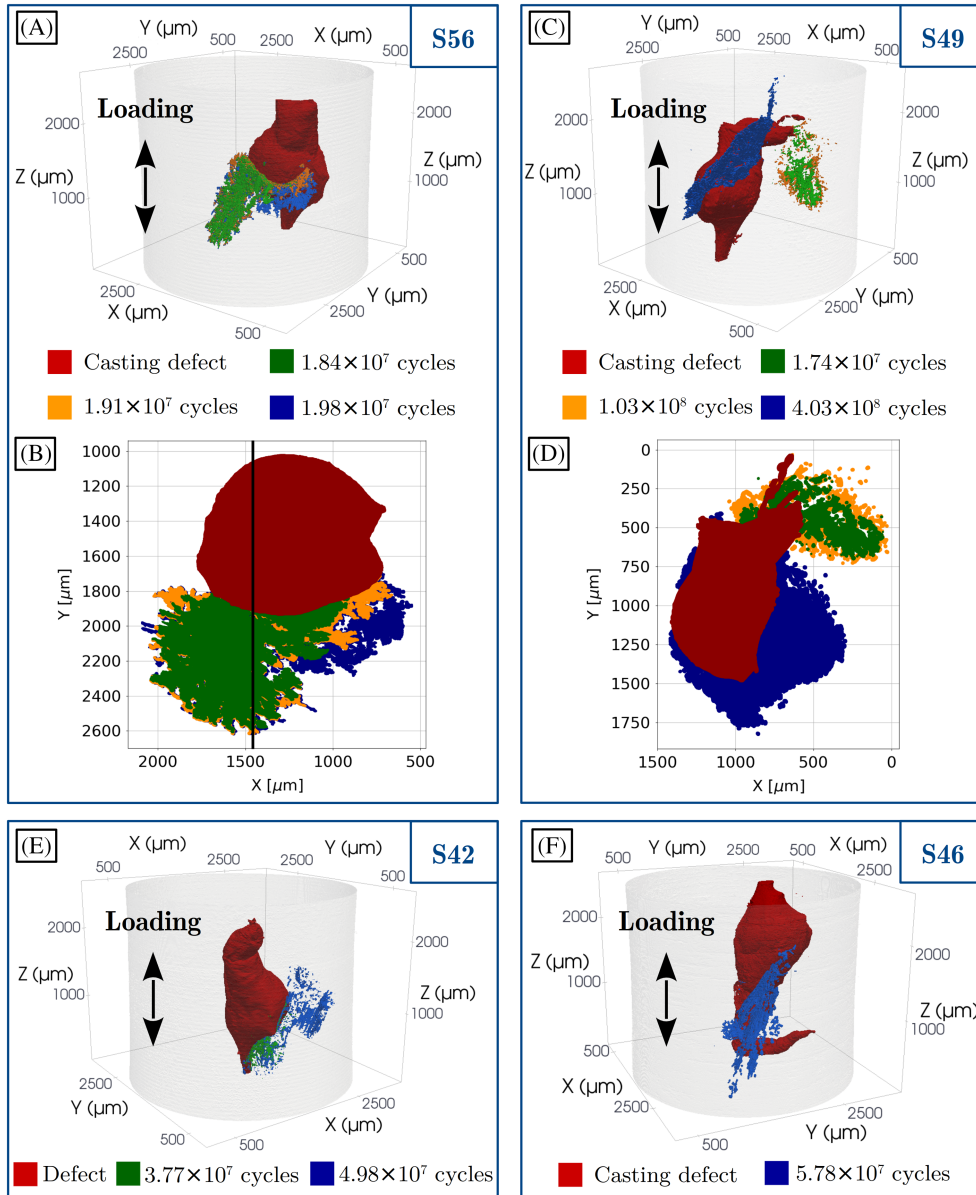
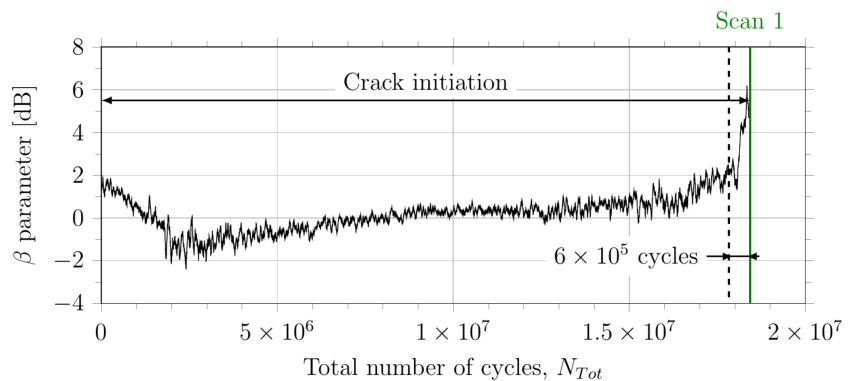


**FIGURE 6** (A), 3D rendering of the defect in red and the internal crack after different number of cycles for the S56 specimen. (B), 2D projected view on plan perpendicular to the loading direction of defect and crack in specimen S56. (C,D), Same type of pictures but for specimen S49. (E,F), 3D rendering of defects and short crack for specimen S42 and S46 (respectively) after different number of cycles [Colour figure can be viewed at [wileyonlinelibrary.com](http://wileyonlinelibrary.com)]

**FIGURE 7** Variation of the nonlinearity parameter during the initiation stage as a function of the number of cycles (specimen S56). Crack initiation detection is indicated at  $1.84 \times 10^7$  cycles by the green vertical line corresponding to the first tomographic scan (scan 1). The vertical dashed line shows the number of cycles at which a significant change in the increase rate of the beta parameter is observed which might indicate “real” crack initiation [Colour figure can be viewed at [wileyonlinelibrary.com](http://wileyonlinelibrary.com)]



ray tomography, infrared thermography, and modal analysis.

## 2.4 | Material and specimen

The studied material is an AlSi7Mg0.6 cast aluminum alloy used to produce automotive or aeronautical components. Specimens are machined from cast rods (produced by CTIF) in which a controlled artificial casting defect was introduced in the central part as explained by Serrano-Munoz et al<sup>33</sup> (Figure 4). A salt (NaCl) particle is used in the mold as a seed for creating a defect when the liquid metal is poured. This, artificial defect has no cohesion with the surrounding Al material and can therefore be considered as a porosity within which the presence of salt might produces environmental conditions different from those of natural defects.<sup>37</sup> A T6 heat treatment is performed on the as cast rods and the material has a coarse dendritic microstructure (equivalent grain size of approximately 500  $\mu\text{m}$ , Figure 4).<sup>37</sup> The central part of the dog bone specimen, where the artificial defect is located, has a 3-mm diameter (Figure 2 and 4).

## 3 | ANALYSIS OF THE EXPERIMENTAL DATA

Four internal cracks were observed in four specimens containing an internal artificial defect. The fatigue test results under fully reversed tension at 20 kHz are presented in Figure 5. Specimens S42, and S46, were tested at TOMCAT beamline of SLS whereas specimens S49 and S56 were tested at PSICHE beamline of synchrotron SOLEIL.

Specimens S42 (Figure 6E) and S49 (Figure 6C,D) with respective defect sizes<sup>‡</sup> of  $\sqrt{A} = 887 \mu\text{m}$  and  $\sqrt{A} = 965 \mu\text{m}$  were loaded at a nominal stress amplitude of 70 MPa. Specimens S46 (Figure 6F) and S56 (Figure 6A,B) with respective defect sizes of  $\sqrt{A} = 939 \mu\text{m}$  and  $\sqrt{A} = 870 \mu\text{m}$  were tested under 75 MPa. To illustrate how the experimental device can be used and its possibilities, two typical specimens are considered hereafter.

On specimen S56, the crack initiation stage was interrupted by the laser vibrometer system after  $1.84 \times 10^7$  cycles. The corresponding detected crack can be observed in green in Figures 6A and 6B. The evolution of the  $\beta$  parameter as a function of the number of cycles for the crack initiation stage is shown in Figure 7. It can be seen that a significant increase (4 dB) in the  $\beta$  parameter value can be observed between  $1.78 \times 10^7$  and  $1.84 \times 10^7$  cycles.

$10^7$  cycles ( $6 \times 10^5$  cycles). This is representative of the short crack initiation. However, further investigations have to be carried out to precisely establish the size of the smallest detectable crack from the  $\beta$  parameter evolution.

After detecting crack initiation, the specimen was tested for 14 propagation sequences of  $10^5$  cycles under the same conditions. All the sequences were relevant, for sake of simplicity, only a few of them are presented hereafter. A more detailed analysis will be published in a next paper. The 3D and projected evolution of the crack can be observed in Figure 6A,B (respectively). The evolution of the temperature variation,  $T$ , averaged in a

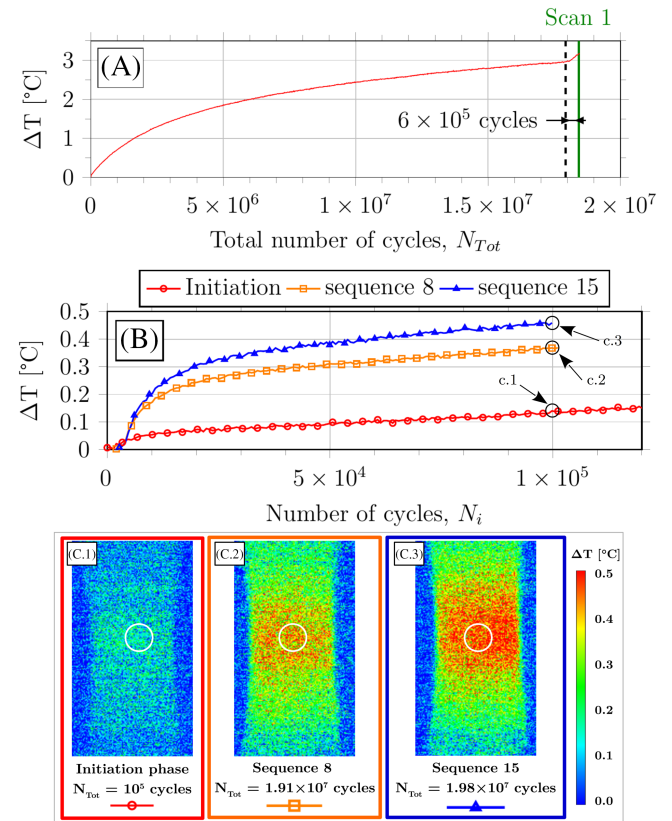


**FIGURE 8** On specimen S56 (A) temperature variation evolution,  $T$ , as a function of the total number of cycles during the crack initiation stage. (B) Temperature variation evolution,  $T$ , as a function of the number of cycles after the beginning of the fatigue tests. The red “Initiation” curve corresponds to a magnified view on the first  $10^5$  cycles of the temperature variation during the initiation stage. Scan 8 (orange) and scan 15 (blue) curves correspond to the states of the internal crack observable in Figure 6A,B and to temperature variation fields observable in (C). (C) Temperature variation field at  $10^5$  cycles after the beginning of (C.1) the initiation stage, (C.2) sequence 8, and (C.3) sequence 15. The white circle represents the area where the temperature variation is averaged and plotted in A and B. Each surrounding frame color and markers correspond to the states of the internal crack observable in Figure 6 A,B and to the averaged temperature variations plotted in A and B [Colour figure can be viewed at [wileyonlinelibrary.com](http://wileyonlinelibrary.com)]

<sup>‡</sup>Where A is the area of the defect projected on the plane perpendicular to the loading axis.<sup>34</sup>

circular zone (1 mm diameter) in the specimen central part is plotted in Figure 8A for the initiation stage and in Figure 8B for two propagation sequences (scans 8 and 15). The temperature variation during the initiation stage (Figure 8A) shows a significant increase  $6 \times 10^5$  cycles before the end of the fatigue test. In Figure 8B, the bottom curve corresponds to a magnified view on the first  $10^5$  cycles of the temperature variation illustrated in Figure 8A (initiation stage: no crack); while “scan 8” and “scan 15” curves correspond, respectively, to the temperature variation because of the propagation of the orange and blue cracks shown in Figure 6A,B. As a consequence of the interrupted fatigue tests, the specimen cools down during the tomographic scans. Therefore, the temperature variation needs to be compared at the same number of cycles after the beginning of cyclic sequences. Figure 8C shows the temperature variation field in the specimen central part  $10^5$  cycles after the beginning of the cyclic sequences. The recorded temperature variations are of the order of  $0.1^\circ\text{C}$  to  $0.5^\circ\text{C}$  (Figure 8B,C). The temperature variations after  $10^5$  cycles of fatigue are also increasing during crack growth (see Figure 8B,C). This can be explained by the increasing plastic dissipation resulting from the enlargement of the reverse cyclic plastic zone at the crack tip due to crack growth.<sup>35,36</sup> However, the temperature variation field in the central part of the specimen (Figure 8C) appears homogeneous because of the combined effect of the slow internal crack growth and the high conductivity of the aluminum alloy.

On specimen S56, the crack detected after  $1.84 \times 10^7$  cycles has an average size of  $\sqrt{A} = 675 \mu\text{m}$ , which is of the order of the grain size of the material ( $500 \mu\text{m}$ ). To the best of the authors knowledge, it is the first time that a thermographic and real-time modal analysis can

be directly correlated to the observation of an internal short crack initiation and growth. Furthermore, at the end of the initiation stage, a strong correlation can be observed between the  $\beta$  increase (Figure 7) and the temperature increase (Figure 8A), which both have a duration of  $6 \times 10^5$  cycles. Using this as an estimated propagation duration between the undamaged state and the detected short crack (green crack in Figure 6 A,B) leads to an average crack growth rate of  $d(\sqrt{A})/dN \approx 10^{-9} \text{ m/cycle}$  which is near the threshold region of crack growth. The last observed stage of the crack (blue stage), after  $1.33 \times 10^6$  cycles of propagation, has an average size of  $\sqrt{A} = 823 \mu\text{m}$ . Between the first (green) and last (blue) crack stage, the crack has an averaged growth rate of  $d(\sqrt{A})/dN \approx 10^{-10} \text{ m/cycle}$  which is, once more, near the nonpropagating threshold. Indeed, the corner of the  $da/dN$  versus  $\Delta K$  curve is of the order of this crack growth rate on metallic alloys. The strong inclination of the short crack with respect to the macroscopic maximum principle stress (Figure 9) is typical of a stage I short crack growth in mode II as already observed in this material.<sup>37,38</sup>

Once initiated, the crack remained arrested for  $1.33 \times 10^6$  cycles (green crack on Figure 6A,B) and propagation resumed in a different direction (orange and blue cracks on Figure 6A,B) probably because of the presence of grain boundaries which are known to be very efficient obstacles at this very low stress level. It is not possible to observe grain boundaries in the reconstructed images in spite of the fact that the phase contrast allows to image the eutectic particles within the alpha matrix. Complementary analysis involving sample sectioning and EBSD are currently being carried out to check this assumption. However, the length of the arrested cracks is consistent with

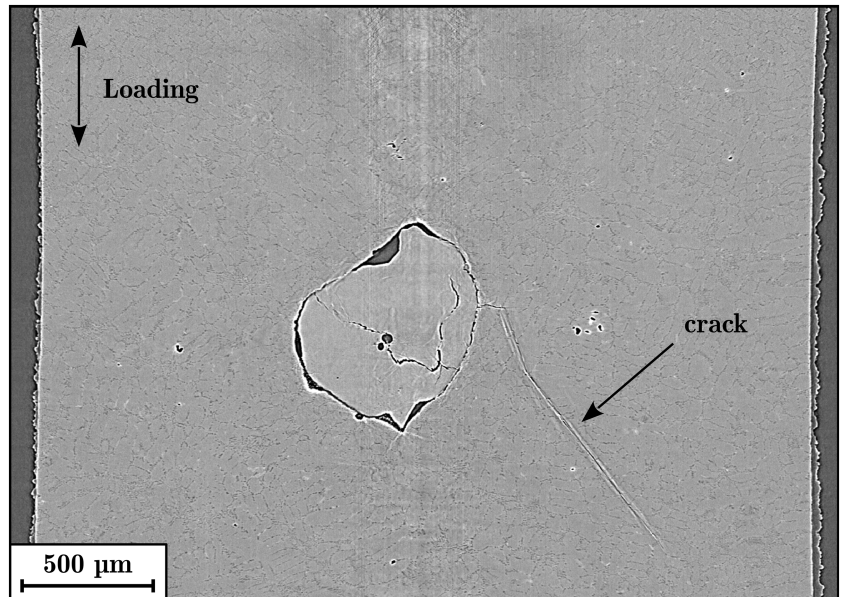


**FIGURE 9** Tomographic slice (corresponding to the black line in Figure 6B) of the internal crack at the end of the initiation stage  $N = 1.84 \times 10^7$  cycles (scan 1) on specimen S56 tested at PISCHE beamline of synchrotron SOLEIL

the measured grain size<sup>37</sup> (mean value 500  $\mu\text{m}$  and standard deviation 190  $\mu\text{m}$ ).

Finally, the very planar crack path observed on Figure 6 (3D) and Figure 9 (2D) is in agreement with cracks propagating in vacuum as observed in other Al alloys.<sup>39</sup> However, solidification defects in cast Al alloy are known to contain some hydrogen and therefore one cannot exclude that this species could play a role on the crack growth by diffusing through the crack to the crack tip.

On specimen S49, first, the initiation of a short crack has been detected and observed (in green on Figure 6C, D) but this crack stopped and another one initiated on the other side of the artificial defect was detected and observed (in blue on Figure 6C,D). From the complex 3D shape and very planar features of the observed cracks, one can assume again a strong interaction of the short crack growth with microstructural barriers (grain boundaries probably). But further investigations are needed to elucidate this point.

## 4 | CONCLUSION AND PROSPECTS

A new experimental setup has been developed. It allows to perform in situ synchrotron ultrasonic fatigue tests, to automatically detect in real-time short crack initiation and to monitor early crack growth on synchrotron beamlines. Compared with previous studies performed at synchrotrons at approximately 20 Hz<sup>12</sup>, this system allows to use very low stress amplitudes ( $\sigma_{\text{max}} \approx \text{Rp}_{0.2}/4$ ).  $10^7$  cycles corresponds to 139 hours at 20 Hz but 500 s only at 20 kHz. With our new experimental setup, the initiation and propagation of an internal fatigue crack has been observed while only surface cracks were observed during similar experiments in LCF or HCF regimes in the same material containing the same type of artificial defects<sup>37</sup>. Reducing the applied stress amplitude to work between HCF and VHCF regime allowed to efficiently promote internal crack initiation.

For the first time, synchrotron tomography has allowed the following:

- a direct observation of internal fatigue crack initiation detected through an in situ real-time FFT analysis,
- Internal microstructurally short crack growth monitoring.

The crack interaction with the microstructure (relatively large grains) during initiation and propagation is strong and requires further investigations. An increasing homogeneous temperature variation in the specimen central part is observed with the expansion of the crack.

Overall, tomographic, modal and infrared thermography analysis are well-correlated and reveal themselves as three complementary nondestructive techniques to study internal microstructurally short crack initiation and propagation.

## ACKNOWLEDGMENTS

This work was carried out within the GIGADEP project grant number ANR-16-CE08-0039. The authors thank the French National Research Agency for its financial support. We acknowledge the Paul Scherrer Institut, Villigen, Switzerland for provision of synchrotron radiation beamtime at beamline TOMCAT of the SLS and Synchrotron SOLEIL, Gif-sur-Yvette, France for beamtime at beamline PSICHE.

## ORCID

Thierry Palin-Luc  <https://orcid.org/0000-0002-2380-0727>

## REFERENCES

1. Murakami Y, Endo T. Effects of small defects on fatigue strength of metals. *International Journal of Fatigue*. 1980;2:23-30.
2. Wilson P, Saintier N, Palin-Luc T, Bergamo S. Isothermal fatigue damage mechanisms at ambient and elevated temperature of a cast Al-Si-Cu aluminium alloy. *International Journal of Fatigue*. 2019;121:112-123.
3. Wang QG, Apelian D, Lados DA. Fatigue behavior of A356-T6 aluminum cast alloys. Part I. Effect of casting defects. *Journal of Light Metals*. 2001;1(1):73-84.
4. Koutiri I, Bellett D, Morel F, Augustins L, Adrien J. High cycle fatigue damage mechanisms in cast aluminium subject to complex loads. *International Journal of Fatigue*. 2013;47:44-57.
5. Ammar HR, Samuel AM, Samuel FH. Effect of casting imperfections on the fatigue life of 319-F and A356-T6 Al-Si casting alloys. *Mater Sci Eng A*. 2008;473:65-75.
6. Luo Y, Wu SC, Hu YN, Fu YN. Cracking evolution behaviors of lightweight materials based on in situ synchrotron X-ray tomography: a review. *Frontiers of Mechanical Engineering*. 2018;13:461-481.
7. Zhang H, Toda H, Qu PC, et al. Three-dimensional fatigue crack growth behavior in an aluminum alloy investigated with in situ high-resolution synchrotron X-ray microtomography. *Acta Mater*. 2009;57(11):3287-3300.
8. Withers PJ, Preuss M. Fatigue and damage in structural materials studied by X-ray tomography. *Annu Rev Mat Res*. 2012;42:81-103.
9. Chapman TP, Kareh KM, Knop M, et al. Characterisation of short fatigue cracks in titanium alloy IMI 834 using X-ray microtomography. *Acta Mater*. 2015;99:49-62.

10. Naragani D, Sangid MD, Shade PA, et al. Investigation of fatigue crack initiation from a non-metallic inclusion via high energy x-ray diffraction microscopy. *Acta Mater.* 2017;137:71-84.
11. Yoshinaka F, Nakamura T, Nakayama S, Shiozawa D, Nakai Y, Uesugi K. Non-destructive observation of internal fatigue crack growth in Ti-6Al-4 V by using synchrotron radiation micro-CT imaging. *International Journal of Fatigue.* 2016;93:397-405.
12. Serrano-Munoz I, Buffiere J-Y, Mokso R, Verdu C, Nadot Y. Location, location & size: defects close to surfaces dominate fatigue crack initiation. *Sci Rep.* 2017;7:45239.
13. Bathias C, Drouillac L, Le Francois P. How and why the fatigue S-N curve does not approach a horizontal asymptote. *International Journal of Fatigue.* 2001;23:143-151.
14. Zuo JH, Wang ZG, Han EH. Effect of microstructure on ultrahigh cycle fatigue behavior of Ti6-Al4-V. *Mater Sci Eng A.* 2008;473:147-152.
15. Nikitin A, Palin-Luc T, Shanyavskiy A. Crack initiation in VHCF regime on forged titanium alloy under tensile and torsion loading modes. *International Journal of Fatigue.* 2016;93:318-325.
16. Bathias C, Pineau A. *Fatigue of Materials and Structures. 1: Fundamentals.* London: ISTE; 2010.
17. Mughrabi H. Specific features and mechanisms of fatigue in the ultrahigh-cycle regime. *International Journal of Fatigue.* 2006;28:1501-1508.
18. Hong Y, Sun C. The nature and the mechanism of crack initiation and early growth for very-high-cycle fatigue of metallic materials—an overview. *Theoretical and Applied Fracture Mechanics.* 2017;92:331-350.
19. Bathias C, Paris PC. *Gigacycle Fatigue in Mechanical Practice.* New York, NY: Dekker; 2005.
20. Murakami Y, Yokoyama NN, Nagata J. Mechanism of fatigue failure in ultralong life regime. *Fatigue Fract Eng Mater Struct.* 2002;25:735-746.
21. Kim J-Y, Jacobs LJ, Qu J, Littles JW. Experimental characterization of fatigue damage in a nickel-base superalloy using nonlinear ultrasonic waves. *J Acoust Soc Am.* 2006;120:1266-1273.
22. Frouin J, Matikas TE, Na JK, Sathish S. In situ monitoring of acoustic linear and nonlinear behavior of titanium alloys during cycling loading. In: *Nondestructive Evaluation of Aging Materials and Composites III.* 1999;3585. International Society for Optics and Photonics:107-117.
23. Cantrell JH, Yost WT. Nonlinear ultrasonic characterization of fatigue microstructures. *International Journal of Fatigue.* 2001;23:487-490.
24. Hikata A, Elbaum C. Generation of ultrasonic second and third harmonics due to dislocations. *Phys Rev.* 1966;144:469-477.
25. Matlack KH, Kim J-Y, Jacobs LJ, Qu J. Review of second harmonic generation measurement techniques for material state determination in metals. *Journal of Nondestructive Evaluation.* 2015;34(1):273.
26. Kumar A, Torbet CJ, Jones JW, Pollock TM. Nonlinear ultrasonics for in situ damage detection during high frequency fatigue. *J Appl Phys.* 2009;106:024904.
27. Campos-Pozuelo C, Vanhille C, Gallego-Juarez JA. Comparative study of the nonlinear behavior of fatigued and intact samples of metallic alloys. *IEEE Trans Ultrason Ferroelectr Freq Control.* 2006;53(1):175-184.
28. Krewerth D, Weidner A, Biermann H. Application of in situ thermography for evaluating the high-cycle and very high-cycle fatigue behaviour of cast aluminium alloy AlSi7Mg (T6). *Ultrasonics.* 2013;53(8):1441-1449.
29. Wagner D, Ranc N, Bathias C, Paris PC. Fatigue crack initiation detection by an infrared thermography method. *Fatigue Fract Eng Mater Struct.* 2009;33:12-21.
30. Guennec B, Ueno A, Sakai T, Takanashi M, Itabashi Y. Effect of the loading frequency on fatigue properties of JIS S15C low carbon steel and some discussions based on micro-plasticity behavior. *International Journal of Fatigue.* 2014;66:29-38.
31. King A, Guignot N, Zerbino P, et al. Tomography and imaging at the PSICHE beam line of the SOLEIL synchrotron. *Rev Sci Instrum.* 2016;87(9):093704.
32. Lovric G, Mokso R, Schlepütz CM, Stampanoni M. A multi-purpose imaging endstation for high-resolution micrometer-scaled sub-second tomography. *Phys Med.* 2016;32(12):1771-1778.
33. Serrano-Munoz I. Influence of casting defects on the fatigue behaviour of an A357-T6 aerospace alloy. November 2014.
34. Murakami Y, Endo M. Quantitative evaluation of fatigue strength of metals containing various small defects or cracks. *Engineering Fracture Mechanics.* 1983;17:1-15.
35. Klingbeil N. A total dissipated energy theory of fatigue crack growth in ductile solids. *International Journal of Fatigue.* 2003;25:117-128.
36. Ranc N, Wagner D, Paris PC. Study of thermal effects associated with crack propagation during very high cycle fatigue tests. *Acta Mater.* 2008;56:4012-4021.
37. Serrano-Munoz I, Buffiere J-Y, Verdu C, Gaillard Y, Mu P, Nadot Y. Influence of surface and internal casting defects on the fatigue behaviour of A357-T6 cast aluminium alloy. *International Journal of Fatigue.* 2016;82:361-370.
38. Brochu M, Verreman Y, Ajersch F, Bouchard D. Propagation of short fatigue cracks in permanent and semi-solid mold 357 aluminum alloy. *International Journal of Fatigue.* 2012;36:120-129.
39. Richard S, Gasquères C, Sarrazin-Baudoux C, Petit J. Coupled influence of microstructure and atmosphere environment on fatigue crack path in new generation Al alloys. *Engineering Fracture Mechanics.* 2010;77:1941-1952.